Two-Degrees-of-Freedom PI^{2}D controller for precise nanopositioning in the presence of hardware-induced constant time delay.

Andres San-Millan[a,*], Vicente Feliu[b], Sumeet S. Aphale[c]

[a] *Instituto de Investigaciones Energeticas y Aplicaciones Industriales (INEI), Campus Universitario de Ciudad Real, 13071 Ciudad Real, Spain*
[b] *Escuela Tecnica Superior de Ingenieros Industriales, Universidad de Castilla-La Mancha, Ciudad Real, 13071 Spain*
[c] *Center for Applied Dynamics Research, School of Engineering, University of Aberdeen, Aberdeen, AB24 3UE, U.K.*

Abstract

The fast and accurate tracking of periodic and arbitrary reference trajectories is the principal goal in many nanopositioning applications. Flexure-based piezoelectric stack driven nanopositioners are widely employed in applications where accurate mechanical displacements at these nanometer scales are required. The performance of these nanopositioners is limited by the presence of lightly damped resonances in their dynamic response and actuator nonlinearities. Closed-loop control techniques incorporating both damping and tracking are typically used to address these limitations. However, most tracking schemes employed use a first-order integrator where a triangular trajectory commonly used in nanopositioning applications necessitates a double integral for zero-error tracking. The phase margin of the damped system combined with the hardware-induced delay deem the implementation of a double-integrator unstable. To overcome this limitation, this paper presents the design, analysis and application of a new control scheme based on the structure of the traditional Two-Degrees-of-Freedom PID controller (2DOF-PID). The proposed controller replaces the integral action of the traditional 2DOF-PID with a double integral action (2DOF-PI^{2}D). Despite its simplicity, the proposed controller delivers superior tracking performance compared to traditional combined damping and tracking control schemes based on well-reported designs such as positive position feedback (PPF), Integral resonant control (IRC), and Positive Velocity and Position Feedback (PVPF). The stability of the control system is analyzed in the presence of a time delay in the system. Experimental results validating the efficacy of the proposed chattering-free control of a piezo-driven nanopositioning system are included.

Keywords: Vibration, Piezoelectric actuators (PEAs), Precision Motion control.

1. Introduction

Micro-/nanopositioning [1] has emerged as a key enabling technology in various scientific fields such as biotechnology [2], fiber optics [3], and atomic force microscopy (AFM) [4]. Among the different actuation methods available, piezoelectric actuators (PEAs) [5, 6] have been extensively adopted in micro-/nanopositioning applications mainly due to their nanometer-scale resolution, high bandwidth, high force density and, absence of backlash and stick–slip [7]. The early models of piezoelectric tube scanners have been replaced by various PEA-driven nanopositioners capable of providing multi-DOF motions [8–11]. Flexure-based nanopositioners are popular due to several key advantages viz: low cross-coupling between motion axes, robust mechanical construction, large motion range and high mechanical bandwidth [12]. However, the two main drawbacks of flexure-based mechanisms are: 1) the nonlinear behavior of the piezoelectric actuators employed to drive the nanopositioner, and 2) the lightly damped resonant modes of the flexible compliant mechanism, which impose an upper bound on the achievable bandwidth - governed predominantly by the first resonant mode of each axis of the nanopositioner.

Since nanopositioners are used for tasks which require both periodic reference trajectory tracking (such as imaging tasks in scanning probe microscopy) and arbitrary aperiodic reference trajectory tracking (such as manipulation and lithography); a high-bandwidth posi-

*Corresponding author
Email addresses:
andres.sanmillan.rodriguez@gmail.com
(Andres San-Millan), vicente.feliu@uclm.es (Vicente Feliu),
s.aphale@abdn.ac.uk (Sumeet S. Aphale)

tioning platform and effective tracking control are required. Resonant modes can be pushed to higher frequencies at the cost of achievable scanning range [13–15]. Therefore, control-based approaches to improving positioning performance is an area of current research interest [16].

Recent examples include resonant control [17], integral resonant control (IRC) [10], and polynomial-based control such as positive position feedback (PPF) [18], and Positive Velocity and Position Feedback (PVPF), which was first introduced as an extension of the PPF, in which the damping controller and the tracking controller were designed independently [19], and then designed simultaneously in [20] by means of selective pole placement to maximize the bandwidth of the nanopositioner. It is important to note that these controllers impart first-order integral tracking action to the overall system and thus are incapable of delivering zero-error tracking performance for trajectories with velocity (triangular or ramp-like). Controllers that provide asymptotic tracking of periodic signals have also been proposed. These are based on the internal model principle (IMP) and use variations of either repetitive control (RC) or iterative learning control (ILC) [11] [21]. It should also be emphasized that in RC, the enhanced performance at the desired periodic frequencies commonly results in deteriorated loop shapes at other frequencies [22], which from a practical point of view means that either the time-period must be constant ($\pm 0.1\%$), or an on-line accurate measurement of the period of the signal is necessary in order to adaptively tune the controller - thereby increasing complexity. Even the recently reported modifications in repetitive control (MRC) [1] cannot guarantee an improved performance at frequencies different from the chosen one, and only provide a robust disturbance rejection against perturbations with frequencies outside the bandwidth of interest. Finally, another drawback of both the RC and the ILC schemes is that they employ information from previous periods to modify the control signal, so it is impossible to track arbitrary aperiodic signals accurately. In order to deal with the nonlinear behavior of the PEAs utilized in the nanopositioners such as the hysteresis, creep and pure time delay, a number of closed-loop control methodologies have been studied without an explicit model of hysteresis or creep, by treating these phenomena as disturbances. Recent examples include robust control [23], sliding-mode control (SMC) [5], resonant control [17], IRC [10], PPF [18], and PVPF [19, 20]. These controllers have shown that hysteretic effects can be effectively compensated by simply incorporating an integral action. Yet, incorporating double integral action has proved difficult mainly due to the system's phase profile and the hardware induced pure time delays.

Yet, for nanopositioning systems, the presence of pure time delays in the system has not been studied in as much depth as the hysteresis and creep phenomena. The existence of a pure time delay (i.e., the presence of a term in the form of $e^{-s\tau}$ in the transfer function of the plant for $\tau > 0$), and its effect on a nanopositioner was first noticed in [24], and has also been studied in [13] and [25] in which a modification to the IRC scheme is utilized to control the nanopositioner. However, these works are principally focused on the mechanical design of the nanopositioner and on the electrical implementation of the control scheme using an analog circuit. It is important to note that in the case of high-bandwidth nanopositioners, the presence of any time delay has an important effect on the stability margins of the closed-loop system and on the performance of the controlled system if the controller is designed based on a model that omits the delay. To the best of our knowledge, only [26] proposes a design methodology that designs a control scheme (PPF controller) for nanopositioners, incorporating this time delay.

PVPF can be treated as a particular case of 2DOF-PID controller as demonstrated in[26]. Therefore, the control design proposed in this paper is termed the 2DOF-PI^{2}D controller because it modifies the transfer function of the block which acts on the tracking error signal by adding a second integral action. The main goals of this design is to outperform the existing control schemes in the following aspects:

1. To track triangular command trajectories with zero steady state error, independent of their fundamental frequency. Other controllers combining a damping controller and integral tracking cannot achieve this (IRC, PPF, and PVPF) or they need an exact knowledge of the time-period of the excitation signals (RC and ILC).
2. Improve the transient response of the closed-loop system (settling time and overshoot) by including the nanopositioner time delay in the controller design procedure, thereby enabling tracking of aperiodic signals without any additional design constraints.

As consequence of this, the scanning rate of any commercial AFM can be effectively doubled by using both slopes of the triangular trajectory to record data (rather than recording for both up and down traverses and averaging out - the typical approach) [16, 27]. The proposed control scheme is simple, the design is synthesized us-

ing pole-placement and the controller is easily implementable in practice.

This paper is organized as follows. Section 2 describes the mathematical model of the piezo-actuated nanopositioner. The 2DOF-PI^{2}D controller design is detailed in Section 3. Section 4 describes the experimental setup. The closed-loop stability analysis of the controller is presented in Section 5, and the experimental results and conclusions are included in Sections 6 and 7.

2. System Modeling

A flexure-based nanopositioner can be interpreted as a Linear Time-Invariant (LTI) Multiple-input Multiple-output (MIMO) system. Since X-Y piezo-actuated flexure-based nanopositioners are usually designed with low cross-coupling between their motion axes, each axis of motion can be treated independently, leading to the following dynamic relationship for each axis:

$$y(s) = g(s)u(s) + f(s) \tag{1}$$

where $u(s)$ and $y(s)$ denote the Laplace transform of the input and output of the system, and where $f(s)$ is the Laplace transform of the perturbation (which describes the combined effects of unmodeled nonlinear dynamics, external perturbations and the artifacts of the neglected coupling). It is important to note that the input to the system, $u(s)$, is the voltage signal applied to the PEA that moves the nanopositioner in that particular axis, and the output of the system, $y(s)$, corresponds to the voltage signal proportional to the displacement achieved, typically recorded using a capacitive displacement sensor. The transfer function $g(s)$, that models the dynamics of the system, can be represented by means of a finite sum of second-order terms given by:

$$g_M(s,\tau) = e^{-\tau s}\sum_{i=1}^{M}\frac{\sigma_i^2}{s^2 + 2\zeta_i\omega_i s + \omega_i^2} \tag{2}$$

where M is the number of resonant modes and is ideally infinite, where σ_i^2 corresponds to the gain of each resonant mode, ζ_i is the damping ratio of each mode, and ω_i is the frequency at which each resonant mode occurs. Note that the exponential term included in the model (2) models the dynamics of the hardware-induced system delay; where τ is the value of the time delay and does not have to be constant. The delay τ of the system is due to two different phenomena: (i) a fixed delay τ_{Fix} due to the latency of the system and the mechanical design of the nanopositioner and (ii) a variable delay proportional to half the sampling time T_s as predicted theoretically in [28, 29]. Thus, τ will be equal to:

$$\tau = \frac{1}{2}T_s + \tau_{Fix} \tag{3}$$

As can be seen from (2), controlling these kinds of systems is a challenging task. On the one hand, the system has an infinite number of poles owing to the infinite modes of vibration, and on the other, since the delay is a transcendental transfer function, it also introduces an infinite number of poles. In order to reduce the complexity of the model (2), it is usually truncated to contain a finite number of modes, and the delay is neglected or approximated by means of a Padé approximation. In several works [20, 25], (2) is truncated at the first mode, since this mode dominates the entire bandwidth of interest. For the system considered in this paper, the first four modes of vibration are modelled ($M = 4$). Furthermore, since the effect of the delay cannot be ignored, it is also included in the dynamic model. It must be highlighted that although only the first mode of vibration is considered in the design of the control scheme proposed in this paper, the remaining three modes of vibration are included in the simulations in order to test the robustness of the proposed controller to unmodeled high-frequency dynamics and spillover effects.

3. 2DOF-PI^{2}D Desgin

As mentioned in the Section 1, several closed-loop control methodologies without an explicit model of the hysteresis have been proposed till date [18–20]. In all these works, the hysteresis is treated as an external disturbance, thus leading to control schemes composed of two nested control loops. The inner loop is utilized impart adequate damping to the resonant mode furnishing higher gain margins that allows the implementation of a high-gain integrator, as accomplished by the outer loop. Since the outer loop is composed of only a first-order integrator, these control schemes can only deliver error-free tracking of step-like trajectories. When these control schemes are utilized to track ramp-like or triangular trajectories, they result in constant steady-state tracking error. Since the raster scanning trajectories typically employed in AFM are triangular, (or triangular with a rounded apex), these trajectories can be viewed as the composition of two ramp signals (one with a positive slope and the other with negative slope), and the aforementioned control schemes cannot track these trajectories with the required accuracy. Additionally, they cannot provide asymptotic tracking either. Though tracking triangular trajectories can be tracked via the internal

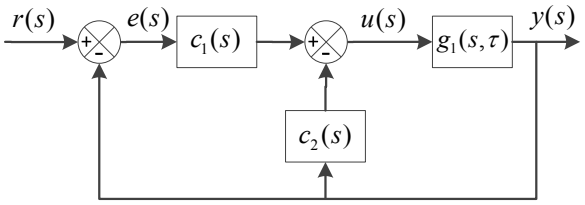

Figure 1: 2DOF PID Control scheme. Tracking controller (c_1) and damping controller (c_2), defined as equations (4) and (5)

model principle using repetitive control [11] or iterative learning control [30], these techniques have several drawbacks: a) they are complicated to design, b) they require several cycles of the signal in order to reduce the tracking error, which deems them inapplicable for non-periodic signals, c) they require perfect knowledge of all the parameters of the system, or in the case of uncertainties, they must be combined with robust control schemes [11] [30]. A simpler approach would be extremely beneficial for such applications.

The proposed control scheme utilizes the control structure shown in Figure 1, in which $g_1(s,\tau)$ is the transfer function of the nanopositioner axis, $c_1(s)$ is the tracking controller and $c_2(s)$ is the damping controller transfer function. In order to achieve asymptotic tracking of ramp signals, the tracking controller $c_1(s)$ has a double integral structure. Being able to track a ramp asymptotically does not mean that is possible to track a triangular trajectory. However, if the triangular trajectory is sufficiently slow (low fundamental frequency), there will be no tracking error along the slopes of the trajectory and only a minimal error at the corners. This result is acceptable if the zone of interest is situated on the slopes of the signal in a raster scan (which is usually the case for most scanning applications).

The transfer functions for $c_1(s)$ and $c_2(s)$, are of the following form:

$$c_1(s) = \frac{N_{11}s + N_{10}}{s^2} \tag{4}$$

$$c_2(s) = \frac{N_{21}s + N_{20}}{s^2 + sD_{21} + D_{20}} \tag{5}$$

Two cases are considered in the proposed design procedure. In the first case, $c_1(s)$ and $c_2(s)$ are designed by simple pole placement considering only the first resonant mode and neglecting the delay ($g_1(s,0)$). In the second case, the delay is included in the equation ($g_1(s,\tau)$), and the positions of the poles designed for the first case are modified in order to compensate for the effect of the delay on the position of the closed-loop poles. Here, ω_1, ζ_1, and σ_1^2 represent the natural frequency, the damping ratio and the gain of the first resonant mode of nanopositioner axis, respectively.

3.1. Design without including delay dynamics

In this case, the closed-loop transfer function has the following expression:

$$\frac{y(s)}{r(s)} = \frac{M_{num}(s)}{M_{den}(s)},$$

where:

$$\begin{aligned}
M_{num}(s) =& s^3\sigma_1^2N_{11} + s^2\sigma_1^2(N_{11}D_{21} + N_{10}) \\
&+ s\sigma_1^2(N_{11}D_{20} + N_{10}D_{21}) + \sigma_1^2N_{10}D_{20} \\
M_{den}(s) =& s^6 + s^5(2\zeta_1\omega_1 + D_{21}) \\
&+ s^4(\omega_1^2 + 2\zeta_1D_{21}\omega_1 + D_{20}) \\
&+ s^3((N_{21} + N_{11}) + D_{21}\omega_1^2 + 2\zeta_1D_{20}\omega_1) \\
&+ s^2(\sigma_1^2(N_{11}D_{21} + N_{20} + N_{10}) + D_{20}\omega_1^2) \\
&+ s\sigma_1^2(N_{11}D_{20} + N_{10}D_{21}) \\
&+ \sigma_1^2N_{10}D_{20}
\end{aligned} \tag{6}$$

$M_{den}(s)$ can be expressed as:

$$M_{den}(s) = s^6+K_5s^5+K_4s^4+K_3s^3+K_2s^2+K_1s+K_0, \tag{7}$$

where:

$$\begin{aligned}
K_5 =& (2\zeta_1\omega_1 + D_{21}) \\
K_4 =& (\omega_1^2 + 2\zeta_1D_{21}\omega_1 + D_{20}) \\
K_3 =& ((N_{21} + N_{11}) + D_{21}\omega_1^2 + 2\zeta_1D_{20}\omega_1) \\
K_2 =& (\sigma_1^2(N_{11}D_{21} + N_{20} + N_{10}) + D_{20}\omega_1^2) \\
K_1 =& \sigma_1^2(N_{11}D_{20} + N_{10}D_{21}) \\
K_0 =& \sigma_1^2N_{10}D_{20}
\end{aligned} \tag{8}$$

It is clear that the coefficients of the characteristic polynomial (7) determine the location of the closed-loop poles of the system. The six poles of the closed-loop can therefore be placed arbitrarily by choosing the values of the coefficients K_i.

The parameters of the controllers $c_1(s)$ and $c_2(s)$ can be solved recursively from (8) leading to the following expressions:

$$
\begin{aligned}
D_{21} =& K_5 - 2\zeta_1\omega_1 \\
D_{20} =& K_4 - \omega_1^2 - 2\zeta_1\omega_1 D_{21} \\
N_{10} =& K_0/(\sigma_1^2 D_{20}) \\
N_{11} =& (K_1 - \sigma_1^2 D_{21} N_{10})/(\sigma_1^2 D_{20}) \\
N_{20} =& (K_2 - D_{20}\omega_1^2 - (D_{21}N_{11} + N_{10})\sigma_1^2)/\sigma_1^2 \\
N_{21} =& (K_3 - D_{21}\omega_1^2 - 2\zeta_1 D_{20} W - N_{11}\sigma_1^2)/\sigma_1^2
\end{aligned} \tag{9}
$$

3.2. Design including the delay dynamics

In this case, the closed-loop transfer function has the following expression:

$$
\frac{y(s)}{r(s)} = \frac{M'_{num}(s)}{M'_{den}(s)},
$$

where:

$$
\begin{aligned}
M'_{num}(s) =& e^{-\tau s}(s^3\sigma_1^2 N_{11} + s^2\sigma_1^2(N_{11}D_{21} + N_{10}) \\
&+ s\sigma_1^2(N_{11}D_{20} + N_{10}D_{21}) + \sigma_1^2 N_{10}D_{20}) \\
M'_{den}(s) =& s^6 + s^5(2\zeta_1\omega_1 + D_{21}) \\
&+ s^4(\omega_1^2 + 2\zeta_1 D_{21}\omega_1 + D_{20}) \\
&+ s^3(e^{-\tau s}\sigma_1^2(N_{21} + N_{11}) + D_{21}\omega_1^2 + 2\zeta_1 D_{20}\omega_1) \\
&+ s^2(e^{-\tau s}\sigma_1^2(N_{11}D_{21} + N_{20} + N_{10}) + D_{20}\omega_1^2) \\
&+ s e^{-\tau s}\sigma_1^2(N_{11}D_{20} + N_{10}D_{21}) \\
&+ e^{-\tau s}\sigma_1^2 N_{10}D_{20}
\end{aligned} \tag{10}
$$

Substituting (9) in (10), and rearranging results in the characteristic equation of the closed-loop transfer function:

$$
\begin{aligned}
M'_{den}(s) =& s^6 + s^5 K_5 + s^4 K_4 + \\
&+ s^3[(8(1 - e^{-\tau s})\zeta_1^2 + 4(e^{-\tau s} - 1))\zeta_1\omega_1^3 \\
&+ (4(e^{-\tau s} - 1)\zeta_1^2 - e^{-\tau s} + 1)K_5\omega_1^2 \\
&+ 2(1 - e^{-\tau s})\zeta_1 K_4\omega_1 + e^{-\tau s}K_3] \\
&+ s^2[(4(1 - e^{-\tau s})\zeta_1^2 + e^{-\tau s} - 1)\omega_1^4 \\
&+ 2(e^{-\tau s} - 1)\zeta_1 K_5\omega_1^3 \\
&+ (1 - e^{-\tau s})K_4\omega_1^2 + e^{-\tau s}K_2] \\
&+ sK_1 e^{-\tau s} \\
&+ K_0 e^{-\tau s}
\end{aligned} \tag{11}
$$

Note that the controller coefficients do not appear explicitly in (11). This expression depends only on the plant parameters and the constants K_i ($\forall\ 0 \leq i \leq 5$). According to (8), controller coefficients are embedded in these constants. The whole design procedure then consists two sequential steps: 1) determining constants K_i that place the six designed closed-loop poles of the system with delay in the desired locations, and 2) obtaining controller coefficients from the K_i's by using the inverse relations (9) that have to be solved sequentially.

To place the six poles of the closed-loop system in the positions p_n (with $1 \leq n \leq 6$), the six conditions $M'_{den}(p_n) = 0$ have to be verified. These can be expressed in a compact matrix form as:

$$
A \cdot K = B \tag{12}
$$

where $K = (K_0, K_1, K_2, K_3, K_4, K_5)^T$, and matrices $B \in \Re^{6x1}$ and $A \in \Re^{6x6}$ depend only on the plant parameters and the desired closed-loop poles, which are:

$$
\begin{aligned}
b_n =& -(4(1 - e^{-\tau p_n})\zeta_1^2 + e^{-\tau p_n} - 1)p_n^2\omega_1^4 \\
&- (8(1 - e^{-\tau p_n})\zeta_1^3 + 4(e^{-\tau p_n} - 1)\zeta_1)p_n^3\omega_1^3 - p_n^6
\end{aligned} \tag{13}
$$

and

$$
\begin{aligned}
a_{n,1} =& e^{-\tau p_n} \\
a_{n,2} =& e^{-\tau p_n} p_n \\
a_{n,3} =& e^{-\tau p_n} p_n^2 \\
a_{n,4} =& e^{-\tau p_n} p_n^3 \\
a_{n,5} =& (1 - e^{-\tau p_n})p_n^2\omega_1^2 + (2 - 2e^{-\tau p_n})\zeta_1 p_n^3\omega_1 + p_n^4 \\
a_{n,6} =& ((4e^{-\tau p_n} - 4)\zeta_1^2 - e^{-\tau p_n} + 1)p_n^3\omega_1^2 \\
&+ (2e^{-\tau p_n} - 2)\zeta_1 p_n^2\omega_1^3 + p_n^5
\end{aligned} \tag{14}
$$

where $1 \leq n \leq 6$.

Linear equation (12) can be solved by inverting matrix A, which would be full rank if it were verified that $p_n \neq p_j$ if $n \neq j$. Once constants K_i have been obtained, the coefficients of controllers $c_1(s)$ and $c_2(s)$ are obtained by substituting in (9). In the case of multiple poles, another invertible matrix A' can be obtained by differentiating conditions (13) and (14) in order to obtain a system of linear equations. The exact location of six closed-loop poles can be defined by following this procedure. However, the transcendental nature of the delay leads to infinitely many characteristic roots in the closed-loop transfer function. In order to complete the design procedure, it is therefore necessary to determine whether the six closed-loop poles designed are dominant over the infinite remaining poles introduced by the delay, i.e., whether the six designed poles are closer to

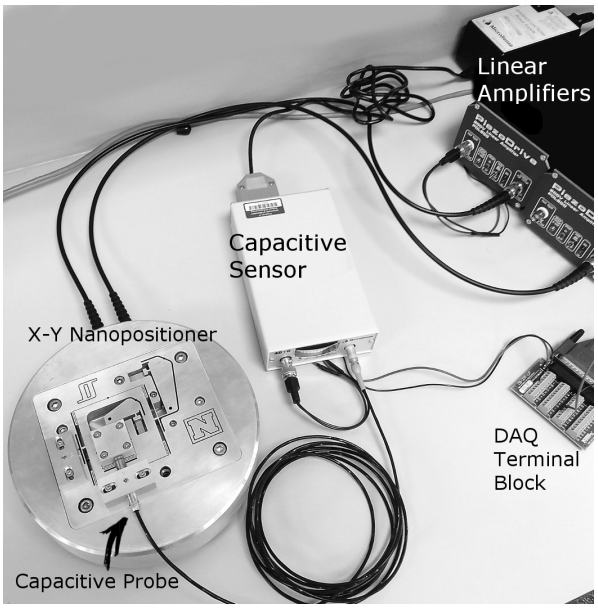

Figure 2: A two-axis serial kinematic nanopositioner, designed at the EasyLab, University of Nevada, Reno, driven by two PiezoDrive 200 V linear amplifiers, with position measured by a Microsense 4810 capacitive sensor.

the imaginary axis than the remaining infinite poles of the system.

Note that this procedure allows the closed-loop poles of the system to be placed in any arbitrary position. However, in this paper, the poles of the closed-loop system are placed by following the design criterion given in [20], in which the desired closed-loop performance is defined by means of a flat band response at low frequencies which rolls off above the resonance frequency. This design criteria is met when the poles of the closed-loop system lie along a circle of radius ω_1 (ω_1 being the natural frequency of the first mode of vibration of the nanopositioner) and are spaced at equal angular distances as in the low pass Butterworth filter (which is often referred to as a "maximally flat magnitude" filter).

4. Experimental platform

In this section, the hardware utilized to test the performance of the proposed control scheme is described. This section also provides details on the identification procedure employed to characterize the experimental platform.

The experimental setup employed in this paper is shown in Figure 2. The nanopositioner (designed at the EasyLab, University of Nevada, Reno, USA) is composed of a flexure XY serial mechanism driven by two PZT stacks with a stroke of 20 μm. The voltage applied to the PZT actuators is provided by two piezoelectric amplifiers which increase the voltage of the control signal by a gain factor of 20 and a bias term of 100V. The nanopositioner delivers translational motions in space which are measured by a Microsense 4810 capacitive displacement sensor and a 2805 measurement probe with a measurement range of ± 50 μm for a corresponding voltage output of ± 10 V. A PCI-6621 data acquisition card from National Instruments installed on a PC running the Real-Time Module from LabVIEW is used to interface between the experimental platform and the control design. The PC utilized is an OPTIPLEX 780 with an Intel(R) Core(TM)2 Duo Processor running at 3.167 GHz and equipped with 2GB of DDR3 RAM memory. The whole system is able to achieve deterministic sampling times of as few as 30×10^{-6} seconds.

The cross-coupling between the two axes was measured and ascertained to be close to -40 dB. Such a small value justifies assuming the axes decoupled (as indicated in Section 2). The $x-$axis of the platform is used to conduct the experiments presented in this work. However, the $y-$axis was biased to +100 V (0 V at the output of the acquisition card) so as to mimic a realistic platform operation.

4.1. Identification of the experimental platform

The work begins with the formulation of the mathematical model of the nanopositioner used to design the controller. The mathematical model of the nanopositioner was identified through the use of small signal frequency response functions (FRFs). FRFs are determined by applying a small-amplitude sinusoidal (0.2 V) chirp signal (from 0.1 to 1800 Hz) as input to the nanopositioner. Both the input and the output signals are then utilized to compute the FRFs by taking the Fourier transform of the recorded data. It should be noted that, when using small amplitudes, the nonlinear effects of the PEAs such as hysteresis are negligible [31]. It should also be noted that, since the capacitive sensor measures relative displacements from a zero point, a new zero point is measured before each experiment in order to avoid any offset in the measurements. In Figure 3, the magnitude and phase responses of the FRF of $g(s)$ are plotted for a sampling time of 50×10^{-6} s.

The chosen frequency range captures the first four resonance modes of the platform (at 716.2, 1235.5, 1294, and 1578 Hz) and also shows that the phase response appears to include a linear term (see the dotted line in Figure 3), suggesting a time delay, which validates the theoretical model (2). The existence of this

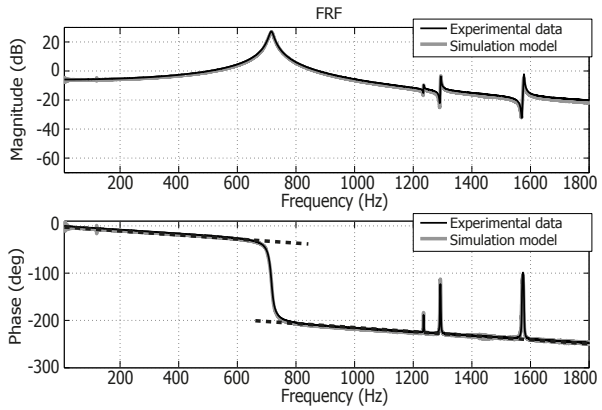

Figure 3: FRF of the experimental platform measured from the input to output displacements

delay, and its effect on nanopositioners, has also been noticed before in [24], [13] and [25]. The procedure used to obtain the transfer function of the system consists of two steps: first, the dominant resonance modes of the transfer function of the system were obtained by using the subspace based modeling technique described in [32], and then the delay was adjusted by minimizing the root mean square error of the phase response.

Expression (3) shows a linear relationship between the sampling time of the system, T_s, and the time-delay τ. The relationship seen between the delay and half the sampling time T_s has been predicted theoretically in [28, 29]. Moreover, the details concerning the identification of the constant term of expression (3), τ_{Fix}, can be found in [26]. This yielded a value of $\tau_{Fix} = 90 \times 10^{-6}$s. Substituting this value and the sampling period $T_s = 30 \times 10^{-6}$s in the axis model expression (3) gives a time-delay $\tau = 105 \times 10^{-6}$s. The identified transfer function is therefore:

$$g_4(s,\tau) = \frac{1.024 \times 10^7 e^{-\tau s}}{s^2 + 99s + 2.025 \times 10^7} + \frac{10000 e^{-\tau s}}{s^2 + 7.76s + 6.026 \times 10^7} + \frac{62500 e^{-\tau s}}{s^2 + 13.01s + 6.61 \times 10^7} + \frac{122500 e^{-\tau s}}{s^2 + 15.86s + 9.83 \times 10^7} \quad (15)$$

The model identified matches the system dynamics well in the frequencies below 1800 Hz and captures the high-frequency dynamics accurately. However, since the first resonant mode dominates the response of the system and the different control schemes analyzed in this paper are developed considering only the first resonant mode, a simple second-order model comprising only the first resonant mode is employed to design the proposed control scheme. The complete model with four resonant modes is used to test the robustness of the proposed controller with regard to the effects of high order dynamics and spillover.

Using an incorrect value of τ (or not considering such time delay at all) would produce a significant error in the matching of the phase plot of the frequency response. Moreover, using an incorrect value of τ in the controller design procedure described in Subsection 3.2 would yield in an ill-tuned controller that would noticeably reduce the closed-loop stability (specially, if the value of the time delay used in the design is lower than the real one).

5. Stability analysis

As stated at the end of Section 3, the proposed design methodology allows the closed-loop poles of the system to be placed in any arbitrary configuration. However, since the stability of the closed-loop system depends on the pole placement employed to design the controller, this paper analyzes the stability of the controller when the closed-loop poles are placed in a pattern mimicking a Butterworth filter. This pole placement pattern is analyzed in [33] in which it is shown to achieve improved tracking performance compared to traditional independent sequential design of damping and tracking controllers.

In this paper, the six closed-loop poles of the system are placed along a circle of radius $R = \omega_1$, spaced at equal angular distances, as in the low pass Butterworth filter (which is often referred to as a 'maximally flat magnitude' filter). The stability of the system is analyzed for two scenarios: a) when the controller is designed by using the equations for systems without delay (8) and (9) and b) when the controller is designed by considering the delay of the system.

In both cases (with and without delay), the controllers designed are computed based on parameters of the first resonant mode of (15), i.e., $g_1(s,\tau)$ and $g_1(s,0)$. Once the controllers have been designed, the complete models of the system with four modes of vibration $g_4(s,\tau)$ and $g_4(s,0)$ are utilized to illustrate that the high order dynamics of the nanopositioner (which are not considered in the design of the controller) do not affect the closed-loop stability of the system. In order to address the issue of an infinite number of poles being introduced by the delay (and in order to simplify the analyses performed in this section), it is desirable to represent an equivalent low degree rational transfer function that approximates the behavior of the delay of the system. The popular method to approximate the effect of the delay is the Padé approximation [34]. The Padé approximation technique has useful features, such as the computational

simplicity and the fitting of time-moments. The Padé approximation is defined as in [35]:

For $n > 1$, the $[n, n]$ Padé approximant is given by:

$$e^{-\tau s} = \frac{p(-s)}{p(s)}, \tag{16}$$

where

$$p(s) = \sum_{k=0}^{n} \binom{n}{k} \frac{(2n-k)!}{(2n)!} s^k. \tag{17}$$

When the second order Padé approximation is utilized to substitute the exponential terms in the transfer function of the closed-loop system, the resulting characteristic equation consists of eight poles (six poles determined by the parameters of the controller employed and two poles introduced by the second order Padé approximation of the system delay).

5.1. *Effect of the delay on the controller by neglecting system delay*

If the controller is designed based only on equations (8) and (9) (system delay neglected) and the closed-loop poles are placed along a circle of radius ω_1, the controller obtained has the following parameters:

$$c_1(s) = \frac{2517s + 2.83 \times 10^6}{s^2} \tag{18}$$

$$c_2(s) = \frac{1.11 \times 10^4 s - 6.371 \times 10^7}{s^2 + s1.381 \times 10^4 + 7.512 \times 10^7} \tag{19}$$

However, if the controller is designed by considering the nominal value of τ ($\tau_0 = 105 \times 10^{-6}$ s), the controller obtained has the following parameters:

$$c_1(s) = \frac{2480s + 2.41 \times 10^6}{s^2} \tag{20}$$

$$c_2(s) = \frac{7812s - 6.01 \times 10^7}{s^2 + s1.28 \times 10^4 + 8.554 \times 10^7} \tag{21}$$

If the controller composed of (18) and (19) is utilized to control the actual plant (with delay), the evolution of the closed-loop poles of the platform is represented in Figure 4 for delays in the range of $[0, 400] \times 10^{-6}$ s.

Figure 4 shows that when the controller is designed by considering the absence of delay in the system, the addition of a time delay to the plant produces a large displacement of the closed-loop poles, even for small delay values. In the case studied, when the delay of the system is equal to 230×10^{-6} s, the controlled system becomes unstable. It will therefore be observed that the stability of the proposed closed-loop system is highly dependent

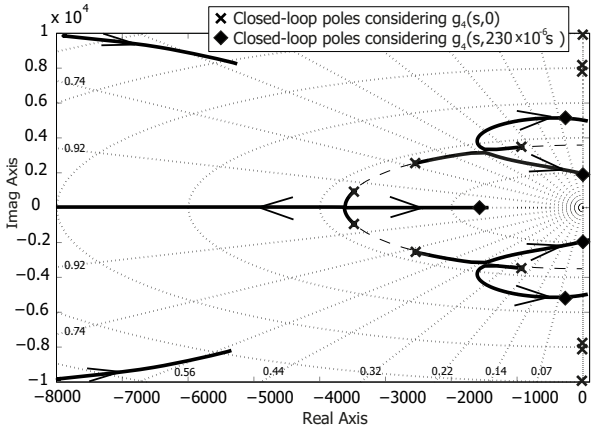

Figure 4: Root contours of the closed-loop system controlled with a design considering no delay. The changing parameter is the delay of the system (circle of radius ω_1 indicated with a dashed line)

on the delay in the system. This characteristic underlines the importance of utilizing equations (13) and (14) in order to compensate for the effect of system delay. It is also important to note that the maximum delay admissible in the system (230×10^{-6} s) is, according to (3), achieved at sampling times as small as 280×10^{-6} s. This upper limit to the maximum admissible delay is determined by the location of the poles corresponding to the first harmonic of the system. Since the poles corresponding to higher modes are placed far from the poles located within the circle of radius $R = \omega_1$, their location is barely affected by the control utilized or the delay introduced in the system. Since these poles never cross the imaginary axis, the proposed control scheme is robust to the spillover effects.

5.2. *Effect of the delay on the controller designed by considering system delay*

When the complete design methodology proposed in this paper is utilized to compute the controller of the system, each different value of the delay yields a new set of parameters for the controller. In this analysis, the delay of the plant is varied in the range $[0, 900] \times 10^{-6}$ s, and the closed-loop poles of the system are plotted. The results are shown in Figure 5.

As seen from Figure 5, if the complete design methodology proposed in this paper is utilized, the six closed-loop poles of the system can be placed arbitrarily, and their position is not disturbed by the effect of the delay. However, the additional poles introduced by the delay (in this case the two poles from the Padé approximation) cannot be controlled. It will also be observed that, as the delay increases, the additional poles intro-

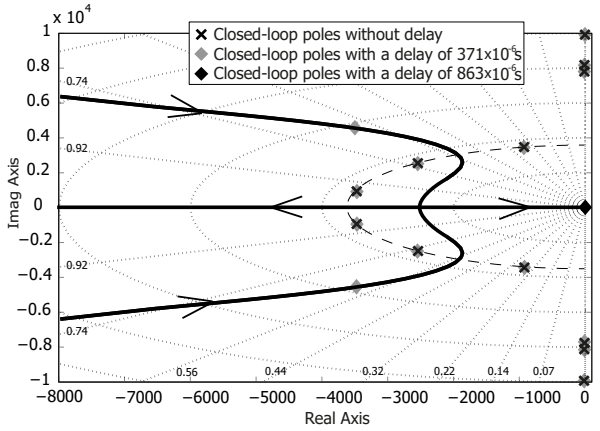

Figure 5: Root contours of the closed-loop system controlled with a design considering delay. The changing parameter is the delay of the system (circle of radius ω_1 indicated with a dashed line)

duced by the delay are displaced closer to the imaginary axis, thus leading to a unstable system for delay values that are greater than 863×10^{-6} s which, according to (3), corresponds to sampling times of 1.546×10^{-3} s.

It is important to note that the increase in the admissible delay is not the only advantage of the proposed control design. The root contours in Figure 4 show that the presence of any value of delay produces a great displacement of the closed-loop poles from their desired position, leading to significant distortion of the closed-loop output. The root contours of Figure 5, meanwhile, show that if the controller is designed by taking the system delay into account, the closed-loop poles remain in their desired positions and the output response therefore remains virtually unaltered. This holds for values of delay within the interval τ=$[0, 370] \times 10^{-6}$ s. For greater values of delay, the additional poles introduced by the delay are placed close enough to the dominant poles to distort the behavior of the closed-loop system, (although this distortion is much smaller that when the controller is designed without taking the delay into account).

This demonstrates that the proposed controller is very sensitive to the effects of the delay, but if the delay is accurately identified, its effects on the placement of the closed-loop poles of the system can be compensated. The delay-included design also delivers improved performance over a larger system delay 863×10^{-6} s when compared to the delay-excluded design 230×10^{-6} s. It is also important to note that the location of the poles corresponding to the higher resonant modes of the system is barely affected

5.3. Impact of the second integrator on the sensitivity function

The proposed control scheme can be interpreted as an extension of the well-reported Positive Velocity and Position Feedback (PVPF) controller, to which a second integral action is added. It is therefore important to discuss the impact of this additional integral action on the behavior of the controlled system. The most informing method is to study the sensitivity of the controlled system. From Figure 1, the closed-loop sensitivity function of the 2DOF-PI^{2}D control scheme is found to be:

$$S(s,\tau) = \frac{e(s)}{r(s)} = \frac{1 + c_2(s)g_4(s,\tau)}{1 + g_4(s,\tau)(c_1(s) + c_2(s))} \qquad (22)$$

The same expression can be employed in the case of the PPF and PVPF controllers, since they share the same block diagram structure. In the case of the IRC controller, however, although the mathematical expression is slightly more complex, the same definition of the sensitivity function is utilized ($S(s,\tau) = \frac{e(s)}{r(s)}$).

Studying the sensitivity of the system is a quantification of the performance limits of any designed control scheme. The double integral action of the $2DOF-PI^2D$ controller decreases the sensitivity at low frequencies (note that sensitivity less than unity means better performance than open loop), but as the integral of the log magnitude of the sensitivity has to remain equal to zero due to the so-called "Waterbed effect" [36, 37], the sensitivity at high frequencies is increased. Sensitivity greater than the unity typically means more ringing and less disturbance rejection at those frequencies. This may lead to instability caused by environmental vibration coupling. The frequency where the unity sensitivity is crossed is denoted as Ω_0.

In order to analyze the sensitivity of the controllers studied in this paper, their closed-loop sensitivity functions are computed, and the integral of the log magnitude of their sensitivity functions are represented in Figure 6. Additionally, different values of delay in the interval $[0, 370] \times 10^{-6}$ s are considered in the system and their effect over the sensitivity function is presented in Figure 7. To evaluate all the controllers against the same design criterion, they are designed to place the closed-loop poles in a Butterworth filter pattern as in [38]. Consequently, each controller is designed to deliver a maximally flat band magnitude response and the bandwidth following the ±3dB criteria is maximized. Additionally, this methodology guarantees a unique solution for the parameters of each controller. Note that only those control schemes capable of delay compensation, i.e., PVPF

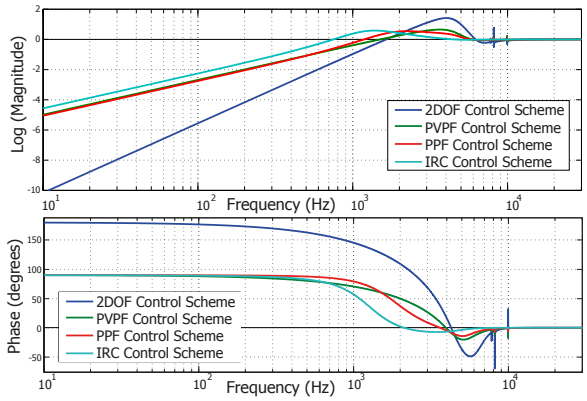

Figure 6: Bode's sensitivity integrals and phase responses for the sensitivity function $S(s,\tau) = \frac{e(s)}{r(s)}$ for all the controllers analysed considering a delay of $\tau = 105 \times 10^{-6}$ s

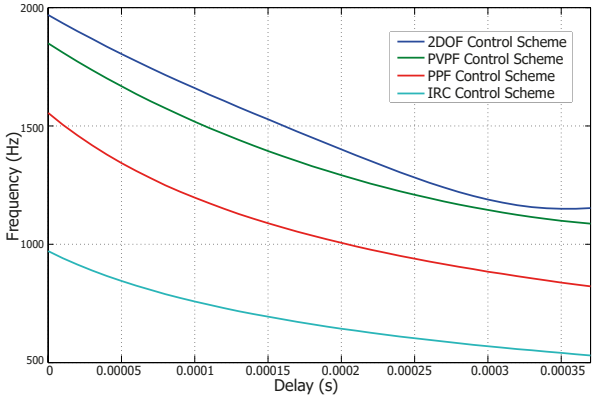

Figure 7: Relationship between Ω_0 (frequency at which the unity sensitivity is crossed) and delay associated with the system

and 2DOF-PI^{2}D, will be able to place their closed-loop poles exactly in that pattern in the presence of a time delay.

The Bode's sensitivity integrals for all the controllers when considering a delay of $\tau = 105{\times}10^{-6}$ s (associated with the sampling time of $30{\times}10^{-6}$ s of the experimental platform) are displayed in Figure 6.

By observing the Bode's sensitivity integrals for all the controllers, it can be concluded that sensitivity reduction at low frequencies leads to sensitivity increase at higher frequencies. Yet, at low frequencies, the 2DOF-PI^{2}D controller delivers better performance of all. Figure 6 shows that the IRC provides $\Omega_0 = 751$ Hz, PPF provides $\Omega_0 = 1184$ Hz, PVPF provides $\Omega_0 = 1505$ Hz, and finally 2DOF-PI^{2}D provides $\Omega_0 = 1646$ Hz.

Since the most representative point of the Bode's sensitivity integrals is the value of Ω_0. The relationship between this point and the value of the delay of the system is shown in in Figure 7 for the four control schemes analyzed.

This analysis shows that, in all the cases, Ω_0 decreases as the delay increases, and that the proposed 2DOF-PI^{2}D controller has the highest value of Ω_0 for each delay associated with the system.

6. Experimental results

The performance of the proposed control scheme is evaluated on the two-axis serial kinematic nanopositioner detailed in Section 4. In order to evaluate the performance of the proposed control scheme, its features are compared in both the time and frequency domains with those of other classical control schemes utilized in nanopositioners, namely: IRC Control Scheme [10], PPF Control Scheme [18] and, PVPF Control Scheme [19]. In order to evaluate all the controllers against the same performance criterion, they were designed considering only the first resonant mode of the nanopositioner axis. Since the IRC and PPF controllers can only be designed for systems without delay, $g_1(s,0)$ was the system to be controlled, and the closed-loop poles were placed in a Butterworth filter pattern with radius $R = \omega_1$ as in [38]. In the case of the PVPF controller, the methodology of [26] was utilized, and the plant was therefore considered by including the actual delay of the system ($g_1(s,\tau)$). In this case, the closed-loop poles were also placed in a Butterworth filter pattern with radius $R = \omega_1$. Finally, $g_1(s,\tau)$ was also considered for the proposed 2DOF-PI^{2}D control scheme, but the closed-loop poles were placed in a Butterworth filter pattern with radius $R = 0.85\omega_1$ in order to remove chattering in the system. The numerical values of the different control schemes utilized are given below:

- IRC control scheme:

$$C_t(s) = \frac{376.8}{s}, \quad C_d(s) = \frac{6360}{s}, \quad d = -0.90 \tag{23}$$

- PPF control scheme:

$$C_t(s) = \frac{973.2}{s}, C_d(s) = \frac{3.689{\times}10^7}{s^2{+}s1.062{\times}10^4{+}3.977{\times}10^7} \tag{24}$$

- PVPF control scheme

$$C_t(s) = \frac{1771}{s}, C_d(s) = \frac{-9450s{+}7.123{\times}10^7}{s^2{+}s1.298{\times}10^4{+}9.687{\times}10^7} \tag{25}$$

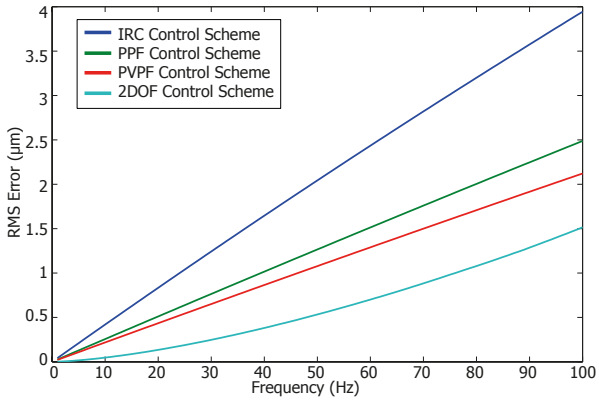

Figure 8: RMS Error produced by the traditional and the proposed 2DOF-PI^{2}D control schemes while tracking ±10 μm triangular trajectories of different frequencies.

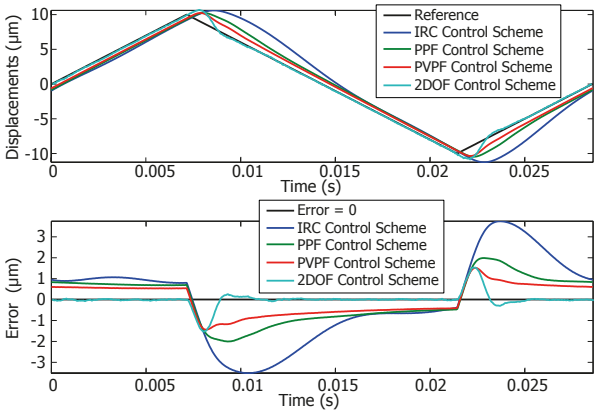

Figure 9: Experimental closed-loop system response and error for various control schemes while tracking a ±10 μm, 35 Hz triangular trajectory.

Control scheme	Max. Error (μm)	RMS Error (μm)
IRC	3.743	1.978
PPF	2.004	1.080
PVPF	1.515	0.728
2DOF-PI^{2}D	1.555	0.271

Table 1: Experimental results for tracking a ±10 μm, 35 Hz triangular trajectory.

6.1. Time-domain Results

In order to quantify the time-domain performance of each control scheme, the platform was subjected to triangular input trajectories of different frequencies, which are typically employed during a raster scan. Additionally, in order to demonstrate the ability of all the controllers to track non-periodic signals, a fifth-order polynomial is also used as a reference trajectory. This applies a "smooth step" to the controlled system ensuring that the value of the jerk (i.e. the rate of change of acceleration) is finite (it is well-know that infinite values of jerk usually leads to adverse affects to the mechanical systems).

6.1.1. Triangular reference trajectory

The group of triangular trajectories with fundamental frequencies between [0,100] Hz and a displacement of ±10 μm were utilized to quantify tracking performance of the discussed control schemes. The corresponding root-mean-square error (RMSE) in the tracking of the triangular reference signal versus the frequency of the reference to be obtained is plotted in Figure 8, for the four control schemes. It is clear that the proposed 2DOF-PI^{2}D control scheme has the lowest RMSE across the entire frequency range. Moreover, in order to illustrate the actual behavior of the system controlled when tracking the reference signal, and to demonstrate the better performance of the proposed 2DOF-PI^{2}D control scheme even in the case of a displacement comprising the full range available, Figure 9 plots recorded time-domain results for a triangular signal of 35 Hz and ±10 μm displacement. Quantitative results are presented in Table 1.

The absence of tracking error along the up and down slopes of the triangular trajectory enables the utilization of both slopes of the trajectory to record data (rather than recording for both up and down traverses and averaging out - the typical approach), thereby effectively doubling the scanning frequency, [27]. Thus, the raster scanning frequency can be set to $f_{raster} = f_s/2(N-1)$, where f_s is the sampling frequency and N is the number of pixels per image [16].

6.1.2. Polynomial reference trajectory

As stated in the Introduction, all the analyzed controllers are capable of delivering error-free tracking of step signals due to the presence of at least first-order (second-order in the case of the 2DOF-PI^{2}D) integral action. In order to illustrate this, an example of a "smooth step" reference is shown in Figure 10). The reference utilized in the experimental setup was generated by using a fifth-order polynomial in order to guarantee a finite value for jerk during all the trajectory.

Figure 10) shows the tracking responses of traditional controllers (23)-(25) and the proposed 2DOF-PI^{2}D controller. It can be seen that all the controllers are capable of reaching a zero-error steady state after some initial settling time. If settling time is denoted by

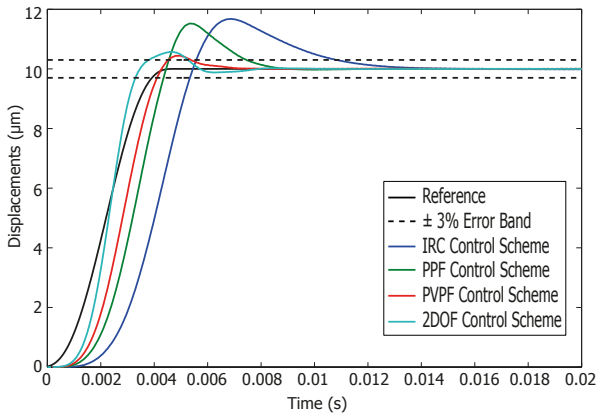

Figure 10: Experimentally recorded tracking response of the various control schemes for a non-periodic 'smooth-step' reference trajectory

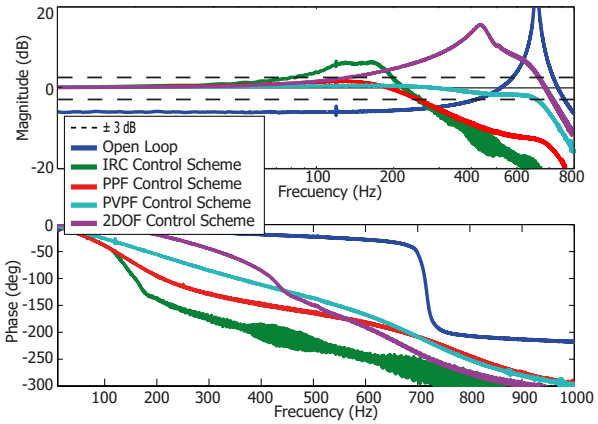

Figure 11: Experimental magnitude and phase response of the open-loop platform and of the closed-loop IRC, PPF, PVFP and 2DOF-PI^{2}D control schemes

t_s and the overshoot as M_p then, the tracking performance achieved can be quantified in descending order as: PVPF ($t_s = 5.35 \times 10^{-3}$s, M_p=4.5%), 2DOF-PI^{2}D ($t_s = 5.25 \times 10^{-3}$s, M_p=5.7%), PPF ($t_s = 7.45 \times 10^{-3}$s, M_p=15.2%), and IRC ($t_s = 10.8 \times 10^{-3}$s, M_p=16.8%).

These results show that only the proposed control scheme is capable of zero tracking error of ramp signals, thus leading to a superior positioning performance when tracking the slopes of the triangular signal. Additionally, the proposed control scheme delivers a superior accuracy in the range of frequencies studied because of its lower rate dependence between the RMSE and the frequency of the signal (it has the least steep ramp in Figure 8). It is important to note that this type of experimentation, in which the controller is designed once and then forced to track triangular signals of a wide range of frequencies, cannot be carried out in the case of controllers based on the internal model principle, such as repetitive control since, as was stated in the Introduction, these controllers require an exact knowledge of the period-time of the excitation signals.

6.2. *Frequency-domain Results*

The well-known criterion of $\pm 3dB$ bandwidth is widely employed in order to quantify the performance of different control schemes as regards nanopositioning systems (because it provides a measure of the achievable tracking bandwidth). However, this criterion is usually employed when the delay of the system is considered to be negligible. In the experimental setup used herewith, the delay cannot be ignored and the simulations conducted in this paper were therefore carried out on the complete model of the experimental platform identified, i.e., $g_4(s, \tau)$, in which the delay value was τ=105 $\times$ 10^{-6}s. Experimental results will validate the simulations.

The results obtained experimentally are presented in Figure 11 and the bandwidths achieved in simulation and in experiments, are provided in Table 2. Experimental and simulated results present good agreement in all the cases (except in the IRC controller, where the noise of the signal produced a more significant difference between simulated and experimental results).

Control scheme	Bandwidth ± 3 dB (Hz)	
	Simulation	Experimental
IRC	118.8	90.4
PPF	246.6	248.6
PVPF	712.2	717.8
2DOF-PI^{2}D	154.4	151.8

Table 2: $\pm 3dB$ bandwidth results with delay in the plant

It is observed that the frequency response of the proposed 2DOF-PI^{2}D control scheme does not follow the flat band response typically achieved when using the low pass Butterworth filter design. This effect is caused by the existence of zeroes in the closed-loop transfer function of the system. Since the zeroes of the closed-loop transfer function cannot be designed arbitrarily, a complete flat band response cannot be achieved (it should be noted that an ideal low pass Butterworth filter does not have any zeroes in its transfer function). However, as stated in Section 3, the proposed design methodology allows the closed-loop poles to be placed arbitrarily; and better patterns for the closed-loop pole placement can therefore be found by means of optimization of the closed-loop response without a loss of gen-

erality.

It is also clear that the proposed control scheme has a relatively lower bandwidth when compared to the PVPF control scheme. However, as can be seen from the time-domain results, providing a high bandwidth does not necessarily result in superior tracking performance for ramp or triangular signals.

6.3. Circular trajectory tracking

Finally, in order to demonstrate the advantages of the proposed control scheme and the ability to track trajectories typically utilized in scanning probe microscopy (aside from triangular ones), simulated results are provided in order to compare the performance of the discussed control schemes for circular trajectory tracking. In order to perform a fair comparison between controllers, simulations were carried out considering no delay in the system (because IRC and PPF cannot compensate the delay). The parameters identified for both axes of the nanopositioner were used in order to mimic a realistic platform operation, and suitable controllers for each axis were designed based on the first resonant mode of each axis.

Figure 12 (a) shows an example of the results obtained when tracking a circular trajectory with a frequency of 200 Hz. From this figure it can be seen that traditional control schemes cannot track high frequency signals and that there is a distortion of the circular trajectory. The eccentricity of the ellipsoid produced when tracking the circular trajectory is utilized in order to quantify the performance of each controller. It is important to note that the eccentricity ϵ is defined as $\epsilon = a/b$, where a and b are the minor and the major axes of the ellipse respectively. Figure 12 (b) shows the relationship between the eccentricity of the trajectories produced by each control scheme and the frequency of the circular reference. It can be seen that the controller proposed in this paper presents a better performance and can track circular trajectories with very small distortion in a wide range of frequencies, whereas the traditional controllers lead to a heavily distorted trajectory even for relatively low frequency references. These results support the efficacy of the proposed 2DOF-PI^{2}D controller and its potential in increasing the scanning frequency of atomic force microscopes.

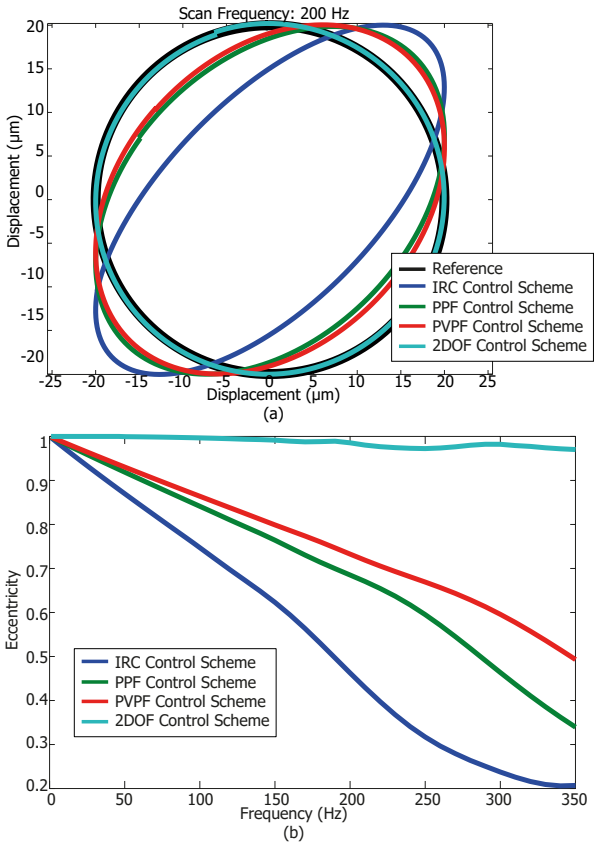

Figure 12: (a) Tracking performance of different control schemes for a circular trajectory with a frequency of 200 Hz. (b) Relationship between the eccentricity of the motion produced by each controller and the frequency of the desired reference signal.

7. Conclusions

This paper proposes a new control scheme based on a two-degrees of freedom PID control, namely 2DOF-PI^{2}D. It also proposes a design methodology for controller parameters by placing the closed-loop poles of the system at selected locations, even in the presence of inherent system delay. The improved tracking performance delivered by the proposed 2DOF-PI^{2}D control scheme has been thoroughly interrogated via an exhaustive set of simulations and validated through experiments. Finally, stability and robustness of the proposed controller in the presence of higher-order system dynamics has also been demonstrated. In future, the proposed control scheme should motivate optimal pole-placement designs for high-speed nanopositioning applications.

References

[1] C. X. Li, G. Y. Gu, M. J. Yang, L. M. Zhu, High-speed tracking of a nanopositioning stage using modified repetitive control, IEEE Transactions on Automation Science and Engineering 14 (3) (2017) 1467–1477.

[2] E. Avci, K. Ohara, C. N. Nguyen, C. Theeravithayangkura, M. Kojima, T. Tanikawa, Y. Mae, T. Arai, High-speed automated manipulation of microobjects using a two-fingered microhand,

IEEE Transactions on Industrial Electronics 62 (2) (2015) 1070–1079.

[3] K. Yoshida, K. Tanaka, T. Tsujimura, Y. Azuma, Assisted focus adjustment for free space optics system coupling single-mode optical fibers, IEEE Transactions on Industrial Electronics 60 (11).

[4] M. Rana, H. Pota, I. Petersen, Performance of sinusoidal scanning with mpc in afm imaging, IEEE/ASME Transactions on Mechatronics 20 (1) (2015) 73–83.

[5] Q. Xu, Design and development of a compact flexure-based XY precision positioning system with centimeter range, IEEE Transactions on Industrial Electronics 61 (2) (2014) 893–903.

[6] H. C. Liaw, B. Shirinzadeh, Robust adaptive constrained motion tracking control of piezo-actuated flexure-based mechanisms for micro/nano manipulation, IEEE Transactions on Industrial Electronics 58 (4) (2011) 1406–1415.

[7] A. Fleming, Design, Modeling and Control of Nanopositioning Systems.

[8] Y. Liu, J. Deng, Q. Su, Review on multi-degree-of-freedom piezoelectric motion stage, IEEE Access (2018) 1–1.

[9] Ultraprecision 6-axis table driven by means of walking drive, CIRP Annals 49 (1) (2000) 299 – 302.

[10] S. S. Aphale, A. J. Fleming, S. O. R. Moheimani, Integral resonant control of collocated smart structures, Smart Materials and Structures 16 (2).

[11] A. A. Eielsen, J. T. Gravdahl, K. K. Leang, Low-order continuous-time robust repetitive control: Application in nanopositioning, Mechatronics 30.

[12] S. O. R. Moheimani, Invited review article: Accurate and fast nanopositioning with piezoelectric tube scanners: Emerging trends and future challenges, Review of Scientific Instruments 79 (7) (2008) –.

[13] Y. K. Yong, B. Bhikkaji, S. O. R. Reza Moheimani, Design, modeling, and FPAA-based control of a high-speed atomic force microscope nanopositioner, IEEE/ASME Transactions on Mechatronics 18 (3) (2013) 1060–1071.

[14] Y. Li, Q. Xu, A novel piezoactuated XY stage with parallel, decoupled, and stacked flexure structure for micro-/nanopositioning, IEEE Transactions on Industrial Electronics 58 (8) (2011) 3601–3615.

[15] Y. Tian, B. Shirinzadeh, D. Zhang, G. Alici, Forward Kinematics and Solution Methodologies for a Flexure-Based Micromanipulator, Springer Berlin Heidelberg, Berlin, Heidelberg, 2008.

[16] Y. R. Teo, Y. K. Yong, A. J. Fleming, A comparison of scanning methods and the vertical control implications for scanning probe microscopy.

[17] H. R. Pota, S. O. R. Moheimani, M. Smith, Resonant controllers for smart structures, Smart Materials and Structures 11 (1).

[18] S. Aphale, B. Bhikkaji, S. Moheimani, Minimizing scanning errors in piezoelectric stack-actuated nanopositioning platforms, IEEE Transactions on Nanotechnology 7 (1) (2008) 79–90.

[19] B. Bhikkaji, M. Ratnam, S. O. R. Moheimani, PVPF control of piezoelectric tube scanners, Sensors Actuators A-Phys. 132 (2) (2007) 700–712.

[20] D. Russell, A. J. Fleming, S. S. Aphale, Simultaneous optimization of damping and tracking controller parameters via selective pole placement for enhanced positioning bandwidth of nanopositioners, Journal of Dynamic Systems Measurement and Control 137 (10).

[21] Y. Li, Q. Xu, Design and Robust Repetitive Control of a New Parallel-Kinematic XY Piezostage for Micro/Nanomanipulation, IEEE/ASME Transactions on Mechatronics 17 (6) (2012) 1120–1132.

[22] X. Chen, M. Tomizuka, New repetitive control with improved steady-state performance and accelerated transient, IEEE Transactions on Control Systems Technology 22 (2) (2014) 664–675.

[23] A. Sebastian, S. Salapaka, Design methodologies for robust nano-positioning, Control Systems Technology, IEEE Transactions on 13 (6) (2005) 868–876.

[24] S. Wadikhaye, B. Bhikkaji, S. Moheimani, Y. K. Yong, Analog implementation of a damping and tracking controller for a high-speed x-y nanopositioner, in: American Control Conference (ACC), 2012, 2012, pp. 3811–3816.

[25] S. P. Wadikhaye, Y. K. Yong, B. Bhikkaji, S. O. Reza Moheimani, Control of a piezoelectrically actuated high-speed serial-kinematic AFM nanopositioner, Smart Materials and Structures 23 (2) (2014) 025030.

[26] A. San-Millan, D. Russell, V. Feliu, S. S. Aphale, A modified positive velocity and position feedback scheme with delay compensation for improved nanopositioning performance, Smart Materials and Structures 24 (7).

[27] B. Bhushan, Springer Handbook of Nanotechnology.

[28] K. Janschek, Mechatronic Systems Design: Methods, Models, Concepts.

[29] C. L. Phillips, H. T. Nagle, Digital Control System Analysis and Design, Prentice Hall, 1995.

[30] Robust iterative learning for high precision motion control through adaptive feedback, Mechatronics 24 (6) (2014) 549 – 561.

[31] K. Leang, Q. Zou, S. Devasia, Feedforward control of piezoactuators in atomic force microscope systems, IEEE Control Systems Magazine 29 (1) (2009) 70–82.

[32] T. McKelvey, H. Akcay, L. Ljung, Subspace-based multivariable system identification from frequency response data, IEEE Transactions on Automatic Control 41 (7) (1996) 960–979.

[33] A. A. Eielsen, M. Vagia, J. T. Gravdahl, K. Y. Pettersen, Damping and tracking control schemes for nanopositioning, IEEE/ASME Transactions on Mechatronics 19 (2) (2014) 432–444.

[34] Y. A. Shamash, Order reduction of linear systems by Padé approximation methods, Ph.D. dissertation, Univ. of London, 1973.

[35] Some frequency-domain approaches to the model reduction of delay systems, Annu. Rev. Control 28 (1) (2004) 65 – 73.

[36] G. Stein, Respect the unstable, IEEE Control Systems 23 (4) (2003) 12–25.

[37] K. J. Aström, R. M. Murray, Feedback systems: an introduction for scientists and engineers, Princeton university press, 2010.

[38] D. Russell, A. San-Millan, V. Feliu, S. S. Aphale, Butterworth pattern based simultaneous damping and tracking controller designs for nanopositioning systems, Frontiers in Mechanical Engineering 2 (2).